Forced dewetting in a capillary tube

Peng Gao[1,2,†], **Ao Liu**[1], **James J. Feng**[3], **Hang Ding**[1] **and Xi-Yun Lu**[1]

[1]Department of Modern Mechanics, University of Science and Technology of China, Hefei, Anhui 230026, China

[2]State Key Laboratory of Fire Science, University of Science and Technology of China, Hefei, Anhui 230026, China

[3]Departments of Chemical and Biological Engineering and Mathematics, University of British Columbia, Vancouver, British Columbia V6T 1Z2, Canada

Liquid films can be entrained when the dewetting velocity attains a threshold, and this dynamical wetting transition has been well studied in the situation of plane substrates. We investigate the forced dewetting in a capillary tube using diffuse-interface simulations and lubrication analysis, focusing on the onset of wetting transition and subsequent interface evolution. Results show that the meniscus remains stable when the displacing rate is below a threshold, beyond which film entrainment occurs and eventually leads to the formation of Taylor bubbles separated by liquid slugs, as has also been observed in the recent experiments of Zhao *et al.* (*Phys. Rev. Lett.*, vol. 120, 2018, 084501). We derive an analytical solution of the critical capillary number, and demonstrate that the wetting transition is accompanied by a vanishing apparent contact angle and an abrupt drop of the contact-line velocity. Both the bubble and slug lengths are found to depend on the capillary number and the wettability of the wall. A theoretical formula for the bubble length is also proposed and compares favourably with numerical and experimental results.

Key words: bubble dynamics, capillary flows, contact lines

1. Introduction

Dynamic wetting or dewetting occurs when one fluid adjacent to a solid substrate is displaced by another one, and is encountered in a variety of natural and industrial problems. It is well known that classical hydrodynamic description of dynamic wetting leads to divergence of viscous stress at the moving contact line (Huh & Scriven 1971), where the liquid–liquid interface intersects the wall. A range of contact-line models have been proposed to relieve the contact-line singularity, such as wall slip and interface diffusion (Bonn *et al.* 2009). The slip model is popular in hydrodynamic theory, which predicts a dynamic contact angle induced by viscous bending of the interface due to the viscous flow close to the contact line (Voinov 1976; Cox 1986). On the other hand, an alternative description of moving contact lines is molecular-kinetic theory, which incorporates a local contact-line friction

† Email address for correspondence: gaopeng@ustc.edu.cn

associated with thermally activation of liquid molecules over the solid (Blake & Haynes 1969; Blake 2006; Seveno *et al.* 2009; Blake & De Coninck 2011). The idea of molecular-kinetic theory has also been employed to interpret the contact-line pinning/depinning on a substrate with defects (e.g. Rolley & Guthmann 2007).

An interesting feature of a moving contact line for partially wetting fluids is the existence of a maximum speed, beyond which a dynamical wetting transition occurs, leading to entrainment of films, drops or gas bubbles (Snoeijer & Andreotti 2013). Film entrainment is the hydrodynamic basis for coating (Weinstein & Ruschak 2004), which may exhibit complex patterns (Thiele 2014; Wilczek *et al.* 2017). In contrast, wetting failure associated with gas entrainment is usually detrimental to industrial applications. We focus on wetting transitions associated with liquid entrainment, and recent progress on gas entrainment can be found in Marchand *et al.* (2012), Vandre, Carvalho & Kumar (2012, 2013, 2014), Chan *et al.* (2013) and Sprittles (2015).

Dynamical wetting transition is typically investigated in the situation of dip coating, in which a plate is withdrawn from a liquid bath at a speed U. The governing parameter is the capillary number $Ca = \mu U / \sigma$, where μ is the liquid viscosity and σ is the surface tension. For small Ca, the problem has been studied under the lubrication approximation. Early investigations of film deposition concerned the situation of complete wetting, with particular interest in the speed dependence of the film thickness (Landau & Levich 1942; Wilson 1982). When the liquid is partially wetting, the critical speed for film entrainment is roughly proportional to θ_e^3, where θ_e is the equilibrium contact angle, as first proposed by de Gennes (1986). This scaling was theoretically demonstrated by Eggers (2004, 2005) for inclined plates and later by Chan, Snoeijer & Eggers (2012) and Qin & Gao (2018) for vertically aligned plates. At the onset of wetting transition, the meniscus behaves as if the liquid were completely wetting, as the apparent contact angle vanishes. In fact, the wetting transition was predicted to be triggered by a saddle-node bifurcation (Snoeijer *et al.* 2007; Chan *et al.* 2012; Tseluiko, Galvagno & Thiele 2014; Wilczek *et al.* 2017), unless the inclination angle of the plate is sufficiently small (Ziegler, Snoeijer & Eggers 2009; Galvagno *et al.* 2014). The critical condition predicted by lubrication theory was confirmed by recent numerical simulations of Gao *et al.* (2016), although the experimentally observed value was overestimated (Snoeijer *et al.* 2006; Delon *et al.* 2008). Beyond the transition, the film evolution is well described by two-dimensional hydrodynamics. The film exhibits complicated morphologies depending on the withdrawal velocity (Snoeijer *et al.* 2006; Gao *et al.* 2016). Specifically, a thick film is obtained for Ca weakly above the critical value, with the thickness selected by the contact line; a further increase of Ca gives rise to the traditional Landau–Levich film (Landau & Levich 1942), but connected to a ridge close to the contact line through a capillary shock. Dynamical wetting transition and film deposition by withdrawing a solid cylinder were investigated by Maleki *et al.* (2007) and Chan, Gueudre & Snoeijer (2011).

The wetting transition in confined geometries, on the other hand, is rarely considered. The contact-line dynamics in a capillary tube was usually studied in the parametric region below the transition in the case of advancing contact lines (Hoffman 1975, 1983; Fermigier & Jenffer 1991). Quéré (1991) investigated the displacement of a drop in a capillary tube and found that a liquid film was entrained beyond a critical velocity. In contrast to planar geometries, Callegari, Calvo & Hulin (2005) reported a dependence on the film thickness of the dewetting velocity of the entrained liquid film. Recently, experiments on forced dewetting were performed by Zhao *et al.* (2018), who found that the entrainment of liquid films would generate a
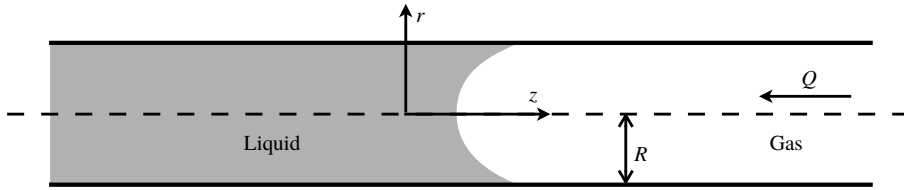
FIGURE 1. Schematic of the axisymmetric two-phase flow in a capillary, where the liquid is displaced by the gas at a constant flow rate Q.

gas finger and eventually cause the formation of Taylor bubbles (Taylor 1961). This process is due to the axisymmetric confinement and differs from the formation of gas fingers induced by Saffman–Taylor instability in Hele-Shaw cells (Saffman & Taylor 1958); in the latter the flow is not confined in the direction parallel to the wall.

In this work, we carry out numerical and theoretical investigations of the forced wetting in a capillary tube. The critical speed for wetting transition is analytically predicted. The simulations not only reproduce the experimental observations of Zhao *et al.* (2018), but also provide detailed flow behaviours, based on which an insightful analysis of the bubble length is performed. The theoretical prediction is in good agreement with the numerical results.

2. Governing equations and numerical method

Consider the two-phase flow in a capillary tube of radius R, as shown in figure 1. The liquid is displaced by the gas with a fixed volume flow rate Q from right to left, and both phases are incompressible and Newtonian. The liquid is partially wetting and the gas–liquid interface intersects the wall at a microscopic contact angle, measured within the liquid. For high-viscosity liquids, the contact angle is assumed to remain at the equilibrium value θ_e, independent of the contact-line speed (Eggers 2005). We further assume that the tube radius is much smaller than the capillary length and the velocity is sufficiently slow, such that both gravitational and inertial effects can be neglected. We expect the interface to behave as a stable meniscus when the flow rate is less than a threshold, beyond which a liquid film is entrained on the tube wall, as typically observed in dip-coating geometries (Snoeijer & Andreotti 2013).

A diffuse-interface method was employed to deal with the deformation of the gas–liquid interface as well as the moving contact line (Jacqmin 2004; Qian, Wang & Sheng 2006; Yue, Zhou & Feng 2010). A phase-field variable ϕ was introduced to distinguish the two fluids, where $\phi = 1$ in the liquid and $\phi = -1$ in the gas. The fluids are mixed and ϕ varies continuously across the interface, which is characterized by a small thickness ϵ. The evolution of pressure p, velocity $\boldsymbol{v}$ and ϕ are governed by the Stokes–Cahn–Hilliard equations,

$$\nabla \cdot \boldsymbol{v} = 0, \tag{2.1}$$

$$-\nabla p + \mu \nabla^2 \boldsymbol{v} + G \nabla \phi = 0, \tag{2.2}$$

$$\partial \phi / \partial t + \boldsymbol{v} \cdot \nabla \phi = \gamma \nabla^2 G. \tag{2.3}$$

Here, the viscosity of the mixed fluids is given by $\mu = (1/2)(1 + \phi)\mu_l + (1/2)(1 - \phi)\mu_g$, which recovers the liquid viscosity μ_l and the gas viscosity μ_g away from the interface; γ is the mobility. The term $G \nabla \phi$ in the momentum equation represents the

effect of interfacial forces, where $G = \Lambda[-\nabla^2\phi + (\phi^2 - 1)\phi/\epsilon^2]$ is the bulk chemical potential, and Λ is the mixing energy density, relating to the interfacial tension σ through $\sigma = 2\sqrt{2}\Lambda/(3\epsilon)$.

We investigate the problem in a reference frame moving to the left with the mean velocity $U = Q/(\pi R^2)$; accordingly, the tube wall moves to the right at the velocity U. This allows one to track the interface evolution in a fixed computational domain. Since the flow is axisymmetric, we employ a rectangular domain of size $R \times 40R$ in the (r, z) plane, which is long enough to avoid any end effect on the interface evolution. Initially, the interface is simply flat and located in the middle of the tube. Parabolic velocity profiles with zero flux across the tube are imposed at the two ends of the domain. The remaining boundary conditions include no-slip condition on the wall and symmetric condition at the axis. In addition, boundary conditions for ϕ are $n \cdot \nabla G = 0$ and

$$\Lambda n \cdot \nabla\phi = \begin{cases} -f'_w(\phi), & \text{on the wall}, \\ 0, & \text{otherwise}, \end{cases} \tag{2.4}$$

where $f_w(\phi) = (1/4)\sigma\phi(\phi^2 - 3)\cos\theta_e$ is the wall free energy. This form of wall energy can guarantee that the profile of ϕ around the contact line is consistent with that across the interface in the bulk, and the contours of ϕ intersect the wall at the angle θ_e (Jacqmin 2000; Yue *et al.* 2010). Moreover, the dynamic contact angle in reality may deviate from the equilibrium one; this effect can be realized by further introducing a wall relaxation in (2.4) (Jacqmin 2000), which was not adopted in the present work for simplicity.

In the following, we scale all lengths by R, velocity by σ/μ_l and time by $\mu_l R/\sigma$. Apart from the contact angle θ_e, the problem is governed by the following dimensionless numbers: the capillary number $Ca = \mu_l U/\sigma$, the viscosity ratio μ_l/μ_g, the Cahn number $Cn = \epsilon/R$ and $S = \sqrt{\gamma\mu_l}/R$. We fixed the viscosity ratio $\mu_l/\mu_g = 50$, which is sufficiently large to render the gas phase negligible, as commonly done for receding contact lines. Note that the contact-line movement is realized through interface diffusion, and S is a dimensionless diffusion length, a microscopic length scale usually encountered in contact-line models. An alternative definition of the diffusion length is $S^* = \sqrt{\gamma\mu^*}/R$ with $\mu^* = \sqrt{\mu_l\mu_g}$ (Yue *et al.* 2010), relating to the present definition through $S = (\mu_l/\mu_g)^{1/4}S^*$. The value of S plays an important role on the contact-line velocity. In reality the microscopic length scale of the contact-line singularity is typically a few nanometres, corresponding to $S \sim O(10^{-5})$ or even smaller for a tube radius of a millimetre (Zhao *et al.* 2018). Such a small length is difficult to resolve in diffuse-interface simulations. We have instead employed $S = 0.005$ and 0.01 in our simulations. As shown by (3.9) below, the critical capillary number scales as $1/\ln S^{-1}$. The large value of S used here would lead to an overestimation of the critical capillary number; an overestimation of the dewetting velocity of liquid films can be expected as well. Nevertheless, the qualitative picture of interface evolution remains the same, with the calculated process of film deposition occurring at larger values of Ca in the simulations. Moreover, we chose $Cn = 0.005$ or 0.01 such that the interface is sufficiently thin and the criteria $Cn < 4S^*$ for the sharp-interface limit is satisfied (Yue *et al.* 2010). Unless otherwise specified, the results presented below were obtained at $Cn = 0.01$ and $S = 0.01$.

The governing equations are solved using a finite-element method coupled with a second-order time stepping scheme (Yue *et al.* 2006; Zhou *et al.* 2010). The mesh is adaptively refined around the interface to capture the steep variation of ϕ. The method has been tested for a wide range of interfacial flows, including the film deposition on a plate (Gao *et al.* 2016).
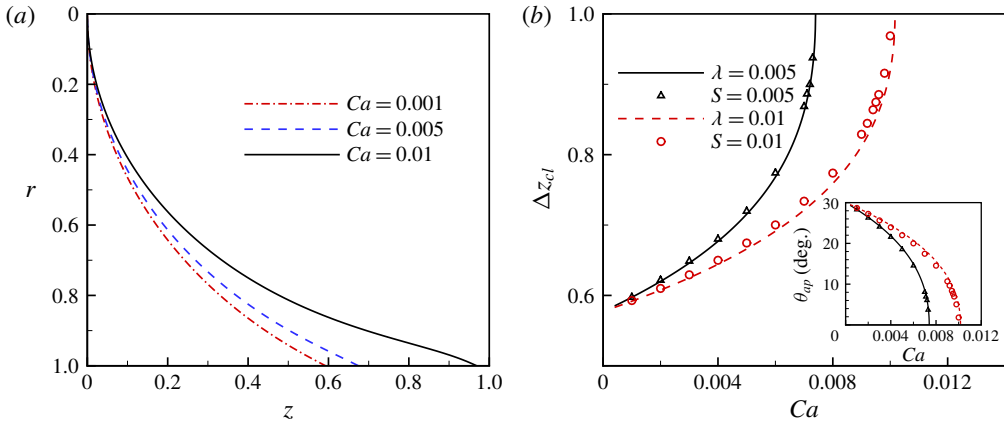
FIGURE 2. (Colour online) (*a*) Representative interfacial profiles when $Ca \leqslant Ca_{cr} = 0.01$ for $\theta_e = 30°$ and $S = 0.01$. The interfaces are shifted such that the tips coincide. (*b*) Distance between the contact line and the meniscus tip, Δz_{cl}, as a function of Ca for $\theta_e = 30°$ and $S = 0.005$ and 0.01. Inset shows the variation of θ_{ap}, relating to Δz_{cl} through (3.1). The symbols represent the diffuse-interface simulations, and the curves correspond to the lubrication theory with the slip length $\lambda = S$.

3. Steady meniscus

When the flow rate is lower than a threshold, or $Ca < Ca_{cr}$, the fluid interface maintains a steady profile after a transient relaxation, and migrates with the average flow velocity, U, with respect to the tube wall. Figure 2(*a*) shows three representative interfacial profiles for $\theta_e = 30°$ and $S = 0.01$. As Ca increases, the interface becomes more curved. The axial distance between the contact line and the meniscus tip, Δz_{cl}, is shown in the figure 2(*b*) as a function of Ca to further characterize the interfacial deformation for $S = 0.005$ and 0.01. It is seen Δz_{cl} increases monotonically from a value determined by θ_e, and the steady solution ceases to exist above a critical capillary number, Ca_{cr}. As expected, a smaller value of S simply leads to a narrower range of Ca for the existence of the steady menisci.

Since $Ca \ll 1$, the macroscopic shape of the meniscus is primarily determined by the balance between surface tension and capillary pressure, while the viscous flow only plays an important role in the vicinity of the contact line. Therefore, it is reasonable to approximate the interface away from the contact line by a spherical cap with an apparent contact angle θ_{ap}, which is related to Δz_{cl} through

$$\Delta z_{cl} = \frac{1 - \sin \theta_{ap}}{\cos \theta_{ap}}, \qquad (3.1)$$

and shown in the inset of figure 2(*b*). The maximum Δz_{cl} of the steady solution is approximately 1, corresponding to $\theta_{ap} = 0$, a criterion usually encountered for wetting transition with receding contact lines (Eggers 2004, 2005; Chan *et al.* 2012).

Following Eggers (2005), an asymptotic solution of the interfacial deformation and the critical capillary number can be obtained for small contact angles based on lubrication theory. The resulting solution is expected to apply to finite contact angles as well, as demonstrated by Qin & Gao (2018). In theoretical analyses, it is convenient to employ a Navier slip model rather than Cahn–Hilliard diffusion to regularize the contact-line singularity. With a slip length λ_s, the ratio of length scales $\lambda \equiv \lambda_s/R \ll 1$ is a counterpart of S in our diffuse-interface simulations. Although there are no explicit rules connecting λ and S, we will show that lubrication theory agrees with diffuse-interface simulations when putting $\lambda = S$, at least for the parameters considered. The thickness of the liquid film is denoted by $h(x)$, where $x \equiv z_{cl} - z$ with z_{cl} being the position of the contact line. The interfaces close to the contact line and away from it, denoted by $h_{in}(x)$ and $h_{out}(x)$ respectively, are treated separately and matched to obtain the full solution. The matching procedure was essentially adopted from Eggers (2005), with a replacement of the curvature of the outer solution, as shown below.

The inner solution is determined by the balance between the surface tension and the viscous force in a region of size $O(\lambda)$. Since $\lambda \ll 1$, the curvature of the tube wall can be neglected, and the contact-line solution on a flat plate can be adopted. This solution was first proposed by Duffy & Wilson (1997), and then extended by Eggers (2005) to allow for slip. For the present purpose, of relevance is the asymptotic form for $\lambda \ll x \ll 1$,

$$h_{in}(x) = \delta^{1/3} \left[\frac{\theta_e^2 \kappa_y}{6\lambda} x^2 + \theta_e b_y x + O(\lambda) \right], \tag{3.2}$$

where

$$\kappa_y(s_1; \delta) = \frac{2^{1/3} \beta^2}{\pi^2 \mathrm{Ai}^2(s_1)}, \qquad b_y(s_1) = -\frac{2^{2/3} \mathrm{Ai}'(s_1)}{\mathrm{Ai}(s_1)}, \tag{3.3}$$

are associated with the curvature and slope of the interface close to the contact line, respectively; $\mathrm{Ai}(s_1)$ is the Airy function with s_1 to be determined and $\delta \equiv 3Ca/\theta_e^3$ is a reduced capillary number. The value of β^2 associated with κ_y has the form

$$\beta^2 = \pi \exp[-1/(3\delta)]/2^{2/3}, \tag{3.4}$$

as first proposed by Eggers (2005) using a matching procedure at the region of $x \gtrsim \lambda$. (Note that ξ is to be replaced by $e\xi$ in (31) and (33) of Eggers (2005).) On the other hand, the outer solution can be well approximated as a spherical cap, which is described as $(1 - h_{out}(x))^2 + (x + \tan\theta_{ap})^2 = 1/\cos^2\theta_{ap}$. For $x \ll 1$, it can be written as

$$h_{out}(x) = \theta_{ap} x + \frac{1}{2} x^2 + O(x^3), \tag{3.5}$$

where we have used the condition $\theta_{ap} \ll 1$ since $\theta_{ap} < \theta_e$ for receding contact lines.

Comparing (3.2) to (3.5), we obtain two matching conditions:

$$\theta_{ap} = \delta^{1/3} \theta_e b_y(s_1), \tag{3.6}$$

$$1 = \frac{\delta^{1/3} \theta_e^2 \kappa_y(s_1; \delta)}{3\lambda}. \tag{3.7}$$

The latter can be rewritten as

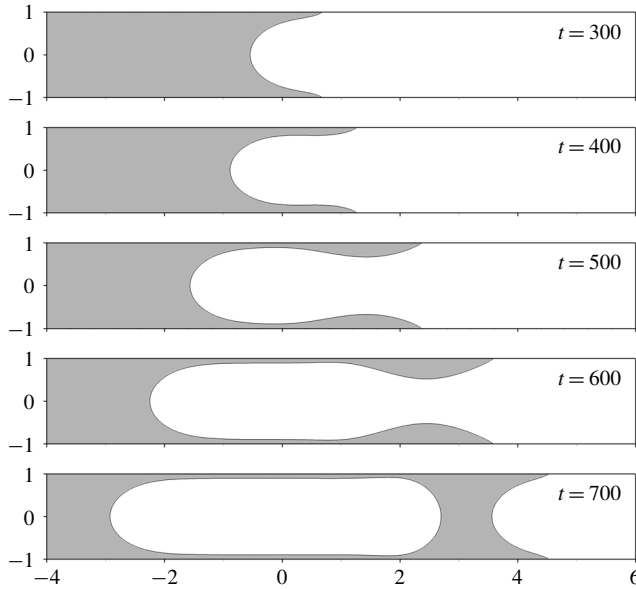$$\mathrm{Ai}^2(s_1) = \frac{\delta^{1/3} \theta_e^2 \exp[-1/(3\delta)]}{2^{1/3} \times 3\pi\lambda}, \tag{3.8}$$

FIGURE 3. Formation of a Taylor bubble for $\theta_e = 50°$ and $Ca = 0.028$, which is slightly larger than $Ca_{cr} = 0.0273$. A moving reference frame is employed such that the tube wall moves to the right with a dimensionless velocity Ca.

which determines s_1 in terms of δ, θ_e and λ. Then substituting s_1 into (3.6) gives θ_{ap} and hence Δz_{cl}. The left-hand side of (3.8) has a global maximum at $s_1 = s_{max} = -1.018\,79\ldots$. When Ca and hence δ increase, the right-hand side of (3.6) may exceed the max $\mathrm{Ai}^2(s_{max})$, and the steady-state solution will be lost. The critical capillary number is accordingly found as

$$Ca_{cr} = \frac{\theta_e^3}{9}\left[\ln\left(\frac{Ca_{cr}^{1/3}\theta_e}{18^{1/3}\pi\mathrm{Ai}^2(s_{max})\lambda}\right)\right]^{-1}. \tag{3.9}$$

Note that the θ_e^3 dependence was also proposed by Quéré (1991), without predicting the logarithmic correction related to θ_e and Ca_{cr}. Furthermore, since $\mathrm{Ai}'(s_{max}) = 0$, the apparent contact angle θ_{ap} vanishes at the threshold, according to (3.6). This is consistent with our numerical simulations, as discussed above.

   A comparison between the lubrication theory and diffuse-interface simulations is presented in figure 2(b) for $\theta_e = 30°$. The separation of length scales is arbitrarily chosen as $\lambda = S$. It is seen that the lubrication theory satisfactorily captures the variation of the interface deformation as well as the critical capillary number, even though the contact angle is not small.

4. Interfacial dynamics above Ca_{cr}

4.1. *Formation of Taylor bubbles*

When $Ca > Ca_{cr}$, the meniscus becomes unstable and a liquid film is entrained on the tube wall. Figure 3 illustrates the interface evolution for $\theta_e = 50°$ and $Ca = 0.028$. Initially, the gas phase penetrates into the liquid, leading to a gas finger. Both the finger tip and the contact line travel at well-defined velocities, but in the opposite
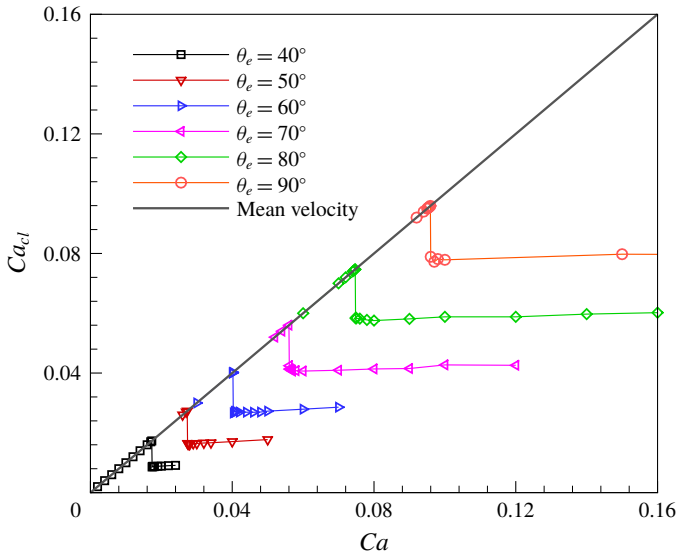
FIGURE 4. (Colour online) Variation of the contact-line velocity relative to the tube wall, Ca_{cl}, as a function of Ca, for representative values of θ_e.

directions in the moving frame. While the gas finger gets elongated, the contact line collects the liquid in the film into a dewetting rim, which grows and then collapses into a liquid slug, leading to the formation of a long bubble, known as a Taylor bubble (Taylor 1961). The newly formed meniscus after the rim collapse remains unstable; therefore this process repeats, eventually giving rise to a train of travelling bubbles. The length of the bubble depends on the flow rate and the wettability of the wall. This process of bubble formation has also been reported by recent experiments of Zhao *et al.* (2018). To quantify the bubble length, a systematic description of the contact-line and gas-finger dynamics is required. The front of the gas finger and the region close to the contact line can be studied separately as the liquid film between them remains uniform.

4.2. *Moving contact line*

Figure 4 shows the contact-line velocity relative to the tube wall, Ca_{cl}, as a function of Ca for representative values of θ_e. The diagonal line $Ca_{cl} = Ca$ marks a contact-line velocity that equals the mean flow velocity. For the solution of stable menisci, Ca_{cl} is simply identical to the mean velocity. At the onset of wetting transition, the contact-line velocity drops suddenly and then stabilizes, once the film is entrained, to a value Ca^* that depends on θ_e but apparently not on the driving flow rate. It corresponds to the dewetting velocity of a film on a solid, which has been extensively studied for the case of a plane substrate (Redon, Brochard-Wyart & Rondelez 1991; Snoeijer & Eggers 2010). Note that Callegari *et al.* (2005) reported a dependence of the dewetting velocity on the film thickness in a capillary tube, where a substantial variation of the film thickness occurs. However, for a fixed contact angle, the range of film thickness can be covered by the present simulations for is much narrower than the experiments of Callegari *et al.* (2005), and the variation of the dewetting velocity is too weak to be resolved.

The present simulations show that wetting transition is supposed to occur at a critical capillary number, Ca_{cr}, larger than the dewetting velocity of a liquid film, Ca^*. In contrast, it was found in the experiments of Zhao *et al.* (2018) that the wetting transition occurred at $Ca = Ca^*$ rather than Ca_{cr}, such that the jump of contact-line velocity was not observed. Interestingly, a similar precritical transition was also encountered in a dip-coating geometry; in the experiments of Snoeijer *et al.* (2006) and Delon *et al.* (2008), wetting transition was observed to occur at a capillary number well below the value predicted by lubrication theory (Snoeijer *et al.* 2007) and numerical simulations (Gao *et al.* 2016). The underlying mechanisms of these inconsistencies remain unclear. Specifically, the contact-line speed was not well captured in Zhao *et al.* (2018) for Ca slightly above the critical value, where the present simulations are focused; further experiments in this parameter region would help elucidate whether or not the velocity jump exists in reality.

4.3. *Dynamics of gas finger*

The dynamics of the gas finger as well as the front of the bubble is characterized by a tip velocity relative to the wall, Ca_b, and a liquid film with thickness h_f. An analysis based on volume conservation reveals that

$$Ca_b = \frac{Ca}{(1-h_f)^2}. \tag{4.1}$$

The film thickness h_f depends solely on Ca_b. Bretherton (1961) first demonstrated that $h_f = 1.34Ca_b^{2/3}$, which is only valid for $Ca_b < 5 \times 10^{-3}$. For larger Ca_b, Aussillous & Quéré (2000) proposed an empirical equation through scaling arguments,

$$h_f = \frac{1.34Ca_b^{2/3}}{1 + 2.5 \times 1.34Ca_b^{2/3}}, \tag{4.2}$$

which fitted the experimental measurements of Taylor (1961) very well. A similar relation was derived theoretically by Klaseboer, Gupta & Manica (2014), with a modification of the coefficient from 2.5 to 2.79. By varying Ca and θ_e, our simulations covered a wide range of Ca_b and h_f, and comparisons with the above expressions are made in figure 5. It is seen in figure 5(*a*) that the film thickness is best predicted by the expression of Aussillous & Quéré (2000). Figure 5(*b*) shows the variation of Ca_b as a function of Ca, where the continuous curve represents (4.1) with h_f given by (4.2). Once again an excellent agreement between theory and numerical simulations is obtained.

4.4. *Bubble length*

The length of the bubble, L_b, defined as the distance between the two end points, depends on Ca and θ_e. As shown in figure 6(*a*), a longer bubble can be realized at smaller contact angles and larger driving velocity. A smaller θ_e corresponds to a slower growth of the rim, enabling a longer time for the gas finger to be elongated; a larger Ca corresponds to a faster invasion of the gas finger, and again leads to a longer bubble.

An estimation of the bubble length can be provided based on the above scenario. The elongation of the finger occurs at a rate of $Ca_b - Ca^*$, and is terminated at the instant Δt when the rim collapses. Within this period, the liquid volume collected by
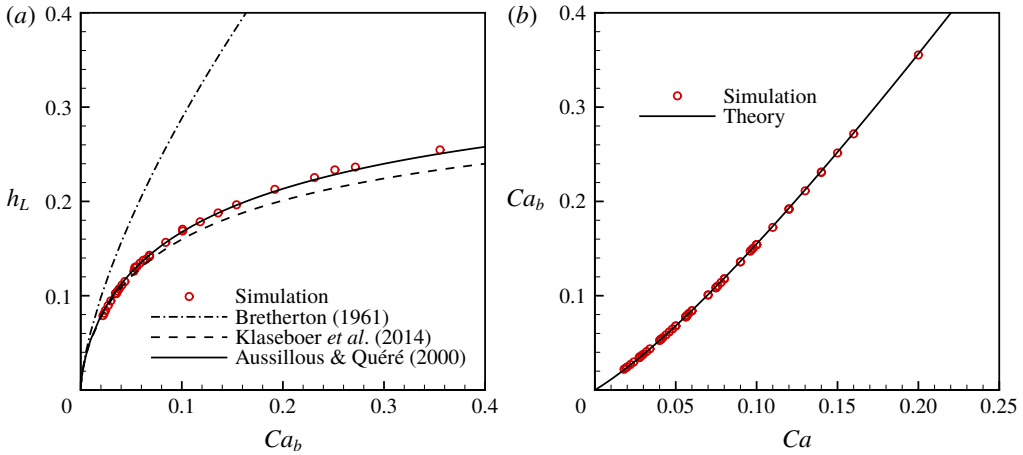
FIGURE 5. (Colour online) Variations of (*a*) the film thickness h_f and (*b*) the bubble velocity Ca_b.

the dewetting rim is $V \approx 2\pi h_f Ca^* \Delta t$, which is also the rim volume. Here we have assumed that the film thickness is much smaller than the tube radius. On the other hand, the rim collapses when its characteristic length is comparable to the tube radius, corresponding to a volume $\alpha\pi$ (or $\alpha\pi R^3$ in dimensional form) with α being a fitting coefficient of $O(1)$. Therefore, by equating the two forms of the volume, we have $\Delta t \approx \alpha/(2h_f Ca^*)$, and eventually

$$L_b = (Ca_b - Ca^*)\Delta t \approx \frac{\alpha}{2h_f}\left(\frac{Ca_b}{Ca^*} - 1\right). \tag{4.3}$$

Since h_f also depends on Ca_b, equation (4.3) indicates that L_b is a function of Ca_b and Ca^*, while Ca plays an implicit role through (4.1) together with (4.2). The effect of contact angle θ_e is solely reflected in Ca^*.

The theoretical results (4.3) coupled with (4.1) and (4.2) are displayed in figure 6(*a*) as the solid curves. We adopted the values of Ca^* from numerical simulations and simply fixed $\alpha = 1$. It is seen that the present theory satisfactorily predicts the bubble length. Due to the large microscopic length used in the present simulations, one may expect the contact-line velocity Ca^* to be considerably larger than the experimental value, as also mentioned earlier. According to (4.3), the bubble length L_b would then be significantly underestimated in the present simulations, as compared to the experiments of Zhao *et al.* (2018). We have compared (4.3) with the experimental data at $\theta_e = 68°$, by adopting $Ca^* \approx 0.014$ extracted from Zhao *et al.* (2018). The present theory reasonably captures the trend of the variation of the bubble length, as shown in the inset of figure 6(*a*).

4.5. *Slug length*

The collapse of the rim produces a liquid slug. Due to the continuing accumulation of the film liquid surrounding the leading bubble, the volume of the slug keeps growing until a new film is entrained behind it. The dependence of the eventual slug length L_s on Ca and θ_e is displayed in figure 6(*b*), which exhibits an opposite trend to L_b. For a
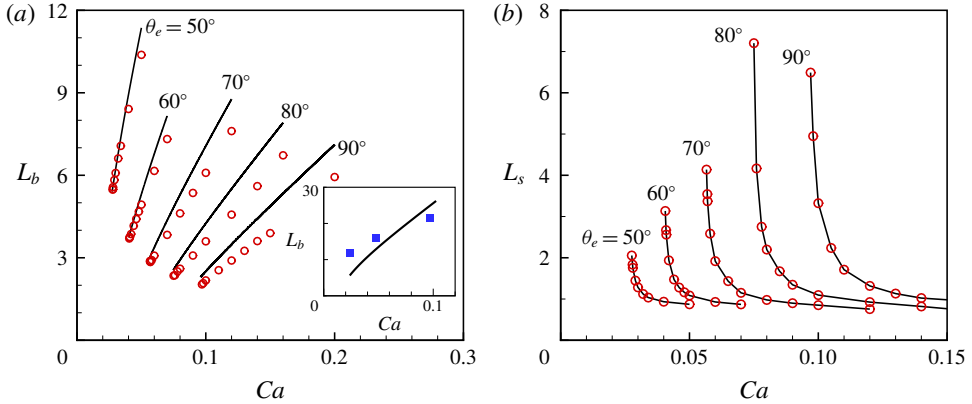
FIGURE 6. (Colour online) (a) Variation of the bubble length L_b as a function of Ca for different contact angles. The lines denote the theoretical prediction (4.3), and the open circles are the simulation results. Inset: comparison of the present theory (line) with the experimental results of Zhao *et al.* (2018) at $\theta_e = 68°$ (squares). We have fixed $\alpha = 1$ in (4.3). (b) Variation of the slug length L_s as a function of Ca.

fixed θ_e, L_s decreases monotonically with Ca. As Ca approaches Ca_{cr} from above, the evolution of the meniscus towards its equilibrium morphology is characterized by a diverging time scale (Snoeijer *et al.* 2007). Therefore, L_s diverges as well. For large Ca, the bubble length decreases to a constant value that is mildly dependent on θ_e. In this situation, the slug is roughly a redistribution of the rim fluid, without the accumulation of the film liquid due to the quick deposition of the new film.

5. Conclusion

We have investigated the dynamic wetting transition in a capillary tube using diffuse-interface simulations and theoretical analysis. Our simulations show that the meniscus remains stable for $Ca < Ca_{cr}$, and Taylor bubbles are generated beyond the threshold, due to the entrainment of the liquid film and subsequent collapse of the rim near the contact line. Both numerical simulations and lubrication theory predict that the wetting transition occurs at vanishing apparent contact angles. An asymptotic solution of Ca_{cr} is obtained. At the onset of wetting transition, the contact-line velocity relative to the tube wall drops discontinuously from the average gas velocity displacing the liquid to a smaller dewetting velocity, which is independent of the gas driving velocity. Both the bubble and slug lengths depend, although oppositely, on Ca and θ_e. An analytical formula for the bubble length is proposed and fits the present numerical results as well as the experimental measurements of Zhao *et al.* (2018).

Acknowledgements

REFERENCES

AUSSILLOUS, P. & QUÉRÉ, D. 2000 Quick deposition of a fluid on the wall of a tube. *Phys. Fluids* **12**, 2367–2371.

BLAKE, T. D. 2006 The physics of moving wetting lines. *J. Colloid Interface Sci.* **299**, 1–13.

BLAKE, T. D. & DE CONINCK, J. 2011 Dynamics of wetting and Kramers' theory. *Eur. Phys. J. Spec. Top.* **197**, 249–264.

BLAKE, T. D. & HAYNES, J. M. 1969 Kinetics of liquid/liquid displacement. *J. Colloid Interface Sci.* **30**, 421–423.

BONN, D., EGGERS, J., INDEKEU, J., MEUNIER, J. & ROLLEY, E. 2009 Wetting and spreading. *Rev. Mod. Phys.* **81**, 739–805.

BRETHERTON, F. P. 1961 The motion of long bubbles in tubes. *J. Fluid Mech.* **10**, 166–188.

CALLEGARI, G., CALVO, A. & HULIN, J. P. 2005 Dewetting processes in a cylindrical geometry. *Eur. Phys. J.* E **16**, 283–290.

CHAN, T. S., GUEUDRE, T. & SNOEIJER, J. H. 2011 Maximum speed of dewetting on a fiber. *Phys. Fluids* **23** (11), 112103.

CHAN, T. S., SNOEIJER, J. H. & EGGERS, J. 2012 Theory of the forced wetting transition. *Phys. Fluids* **24**, 072104.

CHAN, T. S., SRIVASTAVA, S., MARCHAND, A., ANDREOTTI, B., BIFERALE, L., TOSCHI, F. & SNOEIJER, J. H. 2013 Hydrodynamics of air entrainment by moving contact lines. *Phys. Fluids* **25**, 074105.

COX, R. G. 1986 The dynamics of the spreading of liquids on a solid-surface. Part 1. Viscous flow. *J. Fluid Mech.* **168**, 169–194.

DELON, G., FERMIGIER, M., SNOEIJER, J. H. & ANDREOTTI, B. 2008 Relaxation of a dewetting contact line. Part 2. Experiments. *J. Fluid Mech.* **604**, 55–75.

DUFFY, B. R. & WILSON, S. K. 1997 A third-order differential equation arising in thin-film flows and relevant to Tanner's law. *Appl. Math. Lett.* **10**, 63–68.

EGGERS, J. 2004 Hydrodynamic theory of forced dewetting. *Phys. Rev. Lett.* **93**, 094502.

EGGERS, J. 2005 Existence of receding and advancing contact lines. *Phys. Fluids* **17**, 082106.

FERMIGIER, M. & JENFFER, P. 1991 An experimental investigation of the dynamic contact angle in liquid–liquid systems. *J. Colloid Interface Sci.* **146**, 226–241.

GALVAGNO, M., TSELUIKO, D., LOPEZ, H. & THIELE, U. 2014 Continuous and discontinuous dynamic unbinding transitions in drawn film flow. *Phys. Rev. Lett.* **112**, 137803.

GAO, P., LI, L., FENG, J. J., DING, H. & LU, X.-Y. 2016 Film deposition and transition on a partially wetting plate in dip coating. *J. Fluid Mech.* **791**, 358–383.

DE GENNES, P. G. 1986 Deposition of Langmuir–Blodgett layers. *Colloid Polym. Sci.* **264**, 463–465.

HOFFMAN, R. L. 1975 Study of advancing interface. 1. Interface shape in liquid–gas systems. *J. Colloid Interface Sci.* **50**, 228–241.

HOFFMAN, R. L. 1983 A study of the advancing interface. 2. Theoretical prediction of the dynamic contact-angle in liquid gas systems. *J. Colloid Interface Sci.* **94**, 470–486.

HUH, C. & SCRIVEN, L. E. 1971 Hydrodynamic model of steady movement of a solid/liquid/fluid contact line. *J. Colloid Interface Sci.* **35**, 85–101.

JACQMIN, D. 2000 Contact-line dynamics of a diffuse fluid interface. *J. Fluid Mech.* **402**, 57–88.

JACQMIN, D. 2004 Onset of wetting failure in liquid–liquid systems. *J. Fluid Mech.* **517**, 209–228.

KLASEBOER, E., GUPTA, R. & MANICA, R. 2014 An extended Bretherton model for long Taylor bubbles at moderate capillary numbers. *Phys. Fluids* **26**, 032107.

LANDAU, L. D. & LEVICH, B. V. 1942 Dragging of a liquid by a moving plate. *Acta Physicochim. URSS* **17**, 42–54.

MALEKI, M., REYSSAT, E., QUÉRÉ, D. & GOLESTANIAN, R. 2007 On the Landau–Levich transition. *Langmuir* **23**, 10116–10122.

MARCHAND, A., CHAN, T. S., SNOEIJER, J. H. & ANDREOTTI, B. 2012 Air entrainment by contact lines of a solid plate plunged into a viscous fluid. *Phys. Rev. Lett.* **108**, 204501.

QIAN, T., WANG, X.-P. & SHENG, P. 2006 A variational approach to moving contact line hydrodynamics. *J. Fluid Mech.* **564**, 333–360.

QIN, J. & GAO, P. 2018 Asymptotic theory of fluid entrainment in dip coating. *J. Fluid Mech.* **844**, 1026–1037.

QUÉRÉ, D. 1991 On the minimal velocity of forced spreading in partial wetting. *C. R. Acad. Sci. Ser. II* **313**, 313–318.

REDON, C., BROCHARD-WYART, F. & RONDELEZ, F. 1991 Dynamics of dewetting. *Phys. Rev. Lett.* **66**, 715–718.

ROLLEY, E. & GUTHMANN, C. 2007 Dynamics and hysteresis of the contact line between liquid hydrogen and cesium substrates. *Phys. Rev. Lett.* **98**, 166105.

SAFFMAN, P. G. & TAYLOR, G. I. 1958 The penetration of a fluid into a porous medium or Hele–Shaw cell containing a more viscous liquid. *Proc. R. Soc. Lond.* A **245**, 312–329.

SEVENO, D., VAILLANT, A., RIOBOO, R., ADÃO, H., CONTI, J. & DE CONINCK, J. 2009 Dynamics of wetting revisited. *Langmuir* **25**, 13034–13044.

SNOEIJER, J. H. & ANDREOTTI, B. 2013 Moving contact lines: scales, regimes, and dynamical transitions. *Annu. Rev. Fluid Mech.* **45**, 269–292.

SNOEIJER, J. H., ANDREOTTI, B., DELON, G. & FERMIGIER, M. 2007 Relaxation of a dewetting contact line. Part 1. A full-scale hydrodynamic calculation. *J. Fluid Mech.* **579**, 63–83.

SNOEIJER, J. H., DELON, G., FERMIGIER, M. & ANDREOTTI, B. 2006 Avoided critical behavior in dynamically forced wetting. *Phys. Rev. Lett.* **96**, 174504.

SNOEIJER, J. H. & EGGERS, J. 2010 Asymptotic analysis of the dewetting rim. *Phys. Rev.* E **82**, 056314.

SPRITTLES, J. E. 2015 Air entrainment in dynamic wetting: Knudsen effects and the influence of ambient air pressure. *J. Fluid Mech.* **769**, 444–481.

TAYLOR, G. I. 1961 Deposition of a viscous fluid on the wall of a tube. *J. Fluid Mech.* **10**, 161–165.

THIELE, U. 2014 Patterned deposition at moving contact lines. *Adv. Colloid Interface Sci.* **206**, 399–413.

TSELUIKO, D., GALVAGNO, M. & THIELE, U. 2014 Collapsed heteroclinic snaking near a heteroclinic chain in dragged meniscus problems. *Eur. Phys. J.* E **37**, 33.

VANDRE, E., CARVALHO, M. S. & KUMAR, S. 2012 Delaying the onset of dynamic wetting failure through meniscus confinement. *J. Fluid Mech.* **707**, 496–520.

VANDRE, E., CARVALHO, M. S. & KUMAR, S. 2013 On the mechanism of wetting failure during fluid displacement along a moving substrate. *Phys. Fluids* **25**, 102103.

VANDRE, E., CARVALHO, M. S. & KUMAR, S. 2014 Characteristics of air entrainment during dynamic wetting failure along a planar substrate. *J. Fluid Mech.* **747**, 119–140.

VOINOV, O. V. 1976 Hydrodynamics of wetting. *Fluid Dyn.* **11**, 714–721.

WEINSTEIN, S. J. & RUSCHAK, K. J. 2004 Coating flows. *Annu. Rev. Fluid Mech.* **36**, 29–53.

WILCZEK, M., ZHU, J., CHI, L. F., THIELE, U. & GUREVICH, S. V. 2017 Dip-coating with prestructured substrates: transfer of simple liquids and Langmuir–Blodgett monolayers. *J. Phys. Condens. Matter* **29**, 014002.

WILSON, S. D. R. 1982 The drag-out problem in film coating theory. *J. Engng Maths* **16**, 209–221.

YUE, P. T., ZHOU, C. F. & FENG, J. J. 2010 Sharp-interface limit of the Cahn–Hilliard model for moving contact lines. *J. Fluid Mech.* **645**, 279–294.

YUE, P. T., ZHOU, C. F., FENG, J. J., OLLIVIER-GOOCH, C. F. & HU, H. H. 2006 Phase-field simulations of interfacial dynamics in viscoelastic fluids using finite elements with adaptive meshing. *J. Comput. Phys.* **219**, 47–67.

ZHAO, B., PAHLAVAN, A. A., CUETO-FELGUEROSO, L. & JUANES, R. 2018 Forced wetting transition and bubble pinch-off in a capillary tube. *Phys. Rev. Lett.* **120**, 084501.

ZHOU, C. F., YUE, P. T., FENG, J. J., OLLIVIER-GOOCH, C. F. & HU, H. H. 2010 3D phase-field simulations of interfacial dynamics in Newtonian and viscoelastic fluids. *J. Comput. Phys.* **229**, 498–511.

ZIEGLER, J., SNOEIJER, J. H. & EGGERS, J. 2009 Film transitions of receding contact lines. *Eur. Phys. J. Spec. Top.* **166**, 177–180.